PHYSICAL REVIEW B **99**, 155305 (2019)

Fourth-order spin correlation function in the extended central spin model

Nina Fröhling,* Natalie Jäschke,* and Frithjof B. Anders
Lehrstuhl für Theoretische Physik II, Technische Universität Dortmund, Otto-Hahn-Straße 4, 44227 Dortmund, Germany

(Received 25 January 2019; revised manuscript received 22 March 2019; published 16 April 2019)

Spin-noise spectroscopy has developed into a very powerful tool to access the electron spin dynamics. While the spin-noise power spectrum in an ensemble of quantum dots in a magnetic field is essentially understood, we argue that the investigation of the higher-order cumulants promises to provide additional information not accessible by the conventional power-noise spectrum. We present a quantum-mechanical approach to the correlation function of the spin-noise power operators at two different frequencies for small spin bath sizes and compare the results with a simulation obtained from the classical spin dynamics for large number of nuclear spins. This bispectrum is defined as a two-dimensional frequency cut in the parameter space of the fourth-order spin correlation function. It reveals information on the influence of the nuclear-electric quadrupolar interactions on the long-time electron spin dynamics dominated by a magnetic field. For large bath sizes and spin lengths the quantum-mechanical spectra converge to those of the classical simulations. The broadening of the bispectrum across the diagonal in the frequency space is a direct measure of the quadrupolar interaction strength. A narrowing is found with increasing magnetic field indicating a suppression of the influence of quadrupolar interactions in favor of the nuclear Zeeman effect.

DOI: 10.1103/PhysRevB.99.155305

I. INTRODUCTION

Optical spin-noise spectroscopy (SNS) [1] has been established as a minimally invasive probe to study the electron spin dynamics and was originally proposed by Aleksandrov and Zapasskii [2,3]. Off-resonant Faraday rotation measurements were used for nearly perturbation-free measurement of the spin noise in an ensemble of alkali atoms [4], as well as in bulk semiconductors [5–7]. In the absence of an external magnetic field, SNS was able to reveal the influence of the electrical-nuclear quadrupolar interactions on an ensemble of semiconductor quantum dots (QDs) [8] onto the long-time decay [9,10] of the second-order spin correlation function $C_2(t) = \langle S_z(t)S_z\rangle$ as well as on its spin-noise power spectrum [11–17].

The information extracted from the second-order correlation function, however, is limited to macroscopic linear effects by the fluctuation dissipation theorem, if only the thermal equilibrium is considered. For this reason many experimental studies utilized nonequilibrium conditions, generated by radio frequency [18–20] or through periodic laser pulses [21–26].

Higher-order spectra have been studied in context of qubit-based spectroscopy to investigate dynamical decoupling schemes [27,28]. Precise knowledge of the properties of the environmental noise is necessary to utilize quantum dots as qubits. This is why we investigated fourth-order spectra in a quantum dot system.

Applying an external magnetic field to a QD whose strength is exceeding the Overhauser field [29,30] generated by the surrounding fluctuating nuclear spins, however, suppresses the effect of these quadrupolar interactions onto $C_2(t)$ [13]. Yet, quadrupolar interactions play an important role in the understanding of the long-time decay of higher-order spin response functions [31–33] especially at large magnetic fields above 1 T. Since those fourth-order spin correlation functions [31–33] have been investigated in the time domain, it has been suggested [34,35] to extend the conventional SNS to higher-order spin-noise correlations. The third-order spin correlation of the type $C_3(t_1,t_2,t_3) = \langle S_z(t_1)S_z(t_2)S_z(t_3)\rangle$ requires time-reversal symmetry breaking for nonzero values, is imaginary in the time domain in thermal equilibrium and is, therefore, not an observable.

In this paper, we focus on the spectral information of the fourth-order correlation functions [33–35] in the weak measurement regime. It has been established that the real-time fourth-order spin correlation functions contain important information on the field-dependent long-time scale of the decay [31,32] connected to the competition between the nuclear electric quadrupolar couplings and the Zeeman energy [33]. Only little is known about the spectral information of the fourth-order correlation function [34,35]. We demonstrate that the quantum-mechanical fourth-order correlation function in a small spin systems evolves from a set of peaks at discrete excitation energies into a continuous spectrum for large spin systems that is equivalent to a spectrum obtained from a configuration averaged simulation of a classical spin dynamics [25,29,36,37].

In a recent publication Hägele *et al.* proposed an approach to higher-order cumulants and their spectra in the context of a continuous quantum noise measurement [38]. The authors used a time evolution of the density operator by combining the von Neumann equation with a Markovian damping through the environment and a feedback term generated by the continuous measurement of the property of interest. They applied their method to calculate the fourth-order correlation spectrum for two coupled spins in a finite magnetic field.

---

[*] These authors contributed equally to this work.

We present and compare two far simpler approaches based on the linear response theory that is tailored to the nearly perturbation-free optical SNS [6,11,34,35] and is easily applicable to a wide range of scenarios. We are interested in the correlations between the spin-noise power spectrum operator at two different frequencies. For independent noise variables and purely Gaussian noise, the correlation function would factorize and the cumulant [39] would vanish. If the spin dynamics is coherent, this fourth-order spin correlation function yields only nonvanishing contributions at the same frequencies.

We focus on the spin dynamics in a semiconductor quantum dot since it is considered as promising candidate for a quantum bit [40–42]. We analyze the influence of the spin length and number of nuclear spins onto the fourth-order spin-noise spectra using the central spin model (CSM) [43] and its extension to nuclear electric quadrupolar couplings [15,17], which is well suited to describe quantum dot systems [29,44–46]. We show that the spectra calculated by our quantum-mechanical method approach the results obtained by a semiclassical simulation [25,36] in the limit of larger spins and bath sizes. In the opposite limit, we are able to reproduce the higher-order spin spectra in the case of two coupled spins in a finite magnetic field presented in Ref. [38].

The main obstacle for the realization of a quantum bit [40–42] by a QD ensemble is the loss of information, as the electron spin decays over time due to its coupling to a fluctuating environment. While spin decoherence due to free electron motion is suppressed in a quantum dot, the high localization causes the hyperfine interaction between the electron spin and the surrounding nuclear spins to dominate. A detailed investigation of interaction processes influencing the spin dynamics in quantum dots on all time scale is desirable.

The standard SNS was successfully established as a very useful tool to obtain the basis information on the spin dynamics. However, spectral information on very weak interactions such as the nuclear quadrupolar interactions or the influence of the dipole-dipole interactions is lost rather quickly in a finite magnetic field larger than the Overhauser field. We propose to investigate the fourth-order spin-noise spectrum since the shape of the cumulant spectra is significantly altered in the presence of the nuclear quadrupolar interactions even in larger external magnetic fields. Therefore, the fourth-order spin-noise spectrum reveals additional information on the long-time dynamics that is not accessible with the standard SNS. We are able to link the change in the spectroscopic data to the magnetic field dependency of the long-time decay time in higher-order correlations functions [9,31,33].

A short introduction of the model and its semiclassical approximation in Sec. II is followed by the definition of the second- and fourth-order cumulant of the electron spin in Sec. III. Quantum mechanical and classical implementation of the higher-order correlations are presented in Sec. IV. The results are discussed in Sec. V. The influence of the external magnetic field on the spin cumulant is investigated and the classical simulation is discussed as a limit to the quantum-mechanical approach. The quadrupolar interaction is included into the model. Classical and quantum-mechanical treatment will provide an insight into its effect on the higher-order spectrum. A brief summary is given in Sec. VI.

II. MODEL

While an electron spin in a singly negatively charged QD is well isolated from decoherence due to fluctuating charge environments, the strong localization of the electronic wave function increases the coupling between the electron spin and its surrounding nuclear spins. The spin dynamics in the QD is governed by interactions acting on vastly different time scales ranging from the hyperfine interaction (~1 ns) [15,17] to the dipole-dipole interaction (~100 μs) [29]. The quadrupolar interaction caused by electric strain fields and the nuclear spin depends highly on sample growth. We will confine ourselves to the dominating interactions for the spin dynamics in a quantum dot: The hyperfine interaction, the Zeeman interaction of the spins with the external magnetic field $\vec{B}_{\text{ext}}$, and the nuclear-electron quadrupolar interaction.

A. Central spin model

Both the hyperfine interaction as well as the Zeeman energy of the spins in an external magnetic field $\vec{B}_{\text{ext}}$ is described by the Hamiltonian of the central spin model [43]:

$$\tilde{H}_{\text{CSM}} = g_e \mu_B \vec{B}_{\text{ext}} \vec{S} + \mu_N \vec{B}_{\text{ext}} \sum_{k=1}^{N} g_{N,k} \vec{I}_k + \sum_{k=1}^{N} \tilde{A}_k \vec{I}_k \vec{S}. \tag{1}$$

g_e denotes the g factor of the electron, $g_{N,k}$ accounts for the g factor of the kth nucleus, and μ_N is the nuclear magneton. The third term represents the hyperfine interaction between the electronic central spin $\vec{S}$ and the bath comprised N nuclear spins $\vec{I}_k$ conveyed by the coupling constants $\tilde{A}_k$. In negatively charged QDs the hyperfine interaction is isotropic [14]. The fluctuation frequency

$$\omega_{\text{fluc}}^2 = \frac{4}{3} \langle \vec{I}^2 \rangle \sum_{k=1}^{N} \tilde{A}_k^2 \tag{2}$$

of the Overhauser field

$$\vec{B}_N = \sum_{k=1}^{N} \tilde{A}_k \vec{I}_k \tag{3}$$

is used to define the intrinsic time scale $T^* = 1/\omega_{\text{fluc}}$, which describes the short-time electron spin decoherence induced by the fluctuation of the Overhauser field. Typical values of 1–3 ns are found for T^* in experiments, depending on their lateral size [9,15]. The expectation value of the nuclear spin length $\langle \vec{I}^2 \rangle$ takes the value $I(I+1)$ in the quantum-mechanical case while for the classical approximation, we obtain the spin length $\langle \vec{I}^2 \rangle = I^2$.

(In,Ga)As/GaAs QDs contain different isotopes with different spin lengths. While Ga and As isotopes are characterized by a nuclear spin of $I_{Ga} = I_{As} = 3/2$, In has a spin $I_{In} = 9/2$. Therefore, the influence of different I on higher-order correlation functions will be discussed at length in this paper.

The time scale T^* can be utilized to introduce a dimensionless Hamiltonian

$$H = T^* \tilde{H}_{\text{CSM}} \tag{4}$$

with the dimensionless hyperfine coupling constants $a_k = T^* \tilde{A}_k$ and the dimensionless external magnetic field

$\vec{b}_{\text{ext}} = T^* g_e \mu_B \vec{B}_{\text{ext}}$. Assuming that all nuclear spins have the same g factor it is convenient to define

$$\zeta = \frac{g_N \mu_N}{g_e \mu_B}, \tag{5}$$

the ratio between nuclear and electron Zeeman energy. Then, the Hamiltonian takes the dimensionless form

$$H_{\text{CSM}} = \vec{S}\vec{b}_{\text{ext}} + \zeta \vec{b}_{\text{ext}} \sum_{k=1}^{N} \vec{I}_k + \sum_{k=1}^{N} a_k \vec{I}\vec{S}. \tag{6}$$

The hyperfine coupling constants $\tilde{A}_k$ are proportional to the probability of the electron at the location of the kth nucleus, $\tilde{A}_k \propto |\psi_e(\vec{R}_k)|^2$. We assume the envelope of the electron wave function in a d-dimensional quantum dot with the radius L_0 is of the form

$$\psi_e(\vec{r}) = C L_0^{-d/2} \exp\left(-\frac{|\vec{r}|^m}{2L_0^m}\right), \tag{7}$$

with $m = 1$ describing a hydrogenlike and $m = 2$ a Gaussian envelope function. C is a dimensionless normalization constant. With the coupling constant dependent on the probability of an electron being present at the position of the kth nucleus, $\tilde{A}_k \sim |\psi|^2$, the realization of hyperfine coupling constants thus becomes

$$\tilde{A}_k = A_{\max} \exp\left(-\frac{|\vec{r}|^m}{L_0^m}\right). \tag{8}$$

Due to the growth strain in an semiconductor quantum dot the quadrupolar moment of the nucleus interacts with the strained electronic charge distribution in the QD. In case of axial symmetry regarding the local easy axis $\vec{n}_k$, the quadrupolar interaction is represented by the Hamiltonian [17,47,48]

$$H_Q = \sum_k H_q^k = \sum_k q_k (\vec{I}_k \vec{n}_k)^2. \tag{9}$$

The quadrupolar interaction constants q_k are a measure of the quadrupolar interaction strength at the kth nucleus and are quantified by the second derivative of the electron strain field along the easy axis. The local easy axis $\vec{n}_k^z$ have been reported to be at a mean deviation angle of $\bar{\theta} = 23^\circ$ with the growth axis [48] for an $\text{In}_{0.4}\text{Ga}_{0.6}\text{As}$ QD.

B. Semiclassical approximation

In the semiclassical approximation, we replace the quantum-mechanical spin operator with classical vectors and average over all possible initial spin configurations [29,36,37]. In numerical simulations, the integral over all Bloch spheres are replaced by the discrete configuration sample that introduces some finite statistical error that is well controlled by the number of configurations.

The basis of the classical simulation is a set of coupled equations of motion for the central electronic spin $\vec{S}$ and the individual nuclear spins $\vec{I}_k$ [29,37]. Those can be derived as the classical limit from the quantum-mechanical Hamiltonian Eq. (6) via a path integral formalism [36,45]. By solving

$$\frac{d\vec{S}}{dt} = \left(\vec{b}_{\text{ext}} + \sum_k a_k \vec{I}_k\right) \times \vec{S} = \vec{b}_{\text{tot},S} \times \vec{S}, \tag{10}$$

$$\frac{d\vec{I}_k}{dt} = (\zeta \vec{b}_{\text{ext}} + a_k \vec{S}) \times \vec{I}_k = \vec{b}_{\text{tot},I_k} \times \vec{I}_k \tag{11}$$

for different realizations of the initial spin state from the nuclear Gaussian sample space, we can infer the dynamics of the spin expectation values by averaging over the dynamics in each configuration. The mean values of the spin dynamics are interpreted as the time average over consecutive measurements on a single quantum dot.

The dynamics of the electron spin is governed by the external magnetic field as well the hyperfine interaction with the nuclear spins. Those two effects can be merged to one time-dependent effective field $\vec{b}_{\text{tot},S}$ around which the electron spin precesses. The same holds for the differential equations of the nuclear spins, which are influenced by the nuclear Zeeman term $\zeta \vec{b}_{\text{ext}}$ and the Knight field $a_k \vec{S}$.

The classical formalism can also be extended to include the quadrupolar effects on the nuclear spins [47]. Using the Heisenberg equation with H_Q stated in Eq. (9) and assuming commuting classical variables, the effective field $\vec{b}_{\text{tot},I_k}$,

$$\vec{b}_{\text{tot},I_k} = \zeta \vec{b}_{\text{ext}} + a_k \vec{S} + 2q_k (\vec{n}_k \vec{I}_k) \vec{n}_k, \tag{12}$$

can be extended to also comprise the influence of the quadrupolar interaction $2q_k(\vec{n}_k \vec{I}_k)\vec{n}_k$.

The quadrupolar interaction induces an additional precession around the axis $\vec{n}_k$ for each nuclear spin but with a variable precession frequency. The angular frequency is given by the scalar projection of $\vec{I}_k$ onto $\vec{n}_k$ weighted by q_k. Without hyperfine coupling this leads to a precession around a constant $\vec{n}_k$ in which the nuclear Zeeman term acts as a perturbation for small external magnetic fields.

III. CORRELATION FUNCTIONS AND NOISE

Kubo [39] pointed out that cumulants play an role in the probability theory, which is important in quantum-mechanical systems as well as in the thermodynamics. The observation that the moment generating functional

$$\langle e^{\xi X} \rangle = \exp\left(\sum_{n=1}^{\infty} \frac{\xi^n}{n!} \kappa_n\right) = \exp(\langle e^{\xi X} - 1 \rangle_c) \tag{13}$$

with the parameter ξ is linked to the exponentiated series of the nth order cumulant κ_n of the random variable X had a profound impact for the diagrammatic perturbation theory as well as the analysis of the noise [49]. The subscript c refers to the cumulant average.

This concept can be extended to several random variables, which will be replaced by operators in quantum-mechanical calculations. The second-order cumulant of the two variables X_1 and X_2 is defined as

$$\langle X_1 X_2 \rangle_c = \langle X_1 X_2 \rangle - \langle X_1 \rangle \langle X_2 \rangle, \tag{14}$$

which is identical to $\langle X_1 X_2 \rangle$ if the mean average $\langle X_1 \rangle$ vanishes. The same principle can be applied to higher orders [39] and is the basis for the spin-noise analysis presented in this paper.

Here, we are using the Heisenberg operators $S_z(t)$ as variables to define spin-spin correlation functions. In order to access the frequency information for the spin correlation functions of arbitrary order, we introduce the Fourier transformation

$$a(\omega) = \frac{1}{\sqrt{T_m}} \int_{-T_m/2}^{T_m/2} dt\, e^{-\mathrm{i}\omega t} S_z(t), \tag{15}$$

with the measurement time T_m and the measurement starting at $t_0 = -T_m/2$.

If the measuring time T_m is large compared to the characteristic time scale of spin decay, we can apply the limit $T_m \to \infty$ to simplify the mathematical expressions. Note, however, that one has to be careful when applying this limit to avoid unexpected divergence in expressions. We point out below when we have to resort to the original finite measurement time $T_m < \infty$ to remove any ambiguities.

A. Second-order correlation function

The spin-noise experiments in semiconductor QD are generally performed at $T = 4$–6 K, so that the thermal energy is large compared to the energy scale generated by the Overhauser field. Furthermore, we can neglect the equilibrium spin polarization $\langle S_z \rangle$ for a sufficiently low external magnetic field so that the second-order spin-spin autocorrelation function is identical to its cumulant. This second-order autocorrelation function

$$\tilde{C}_2(t_1, t_2) = \langle S_z(t_1) S_z(t_2) \rangle \tag{16}$$

describes the correlation between the z-component of the spin at the start of the measurement t_1 and at a time t_2.

Since experiments on spin noise in quantum dots are usually performed in the linear response regime, we assume that the system is in equilibrium and the Hamiltonian commutes with the density operator. This implies that the system is translationally invariant in time, the correlation function only depends on the relative time $\tau = t_1 - t_2$, and therefore can be expressed as $C_2(\tau) = \langle S_z(\tau) S_z(0) \rangle$. This holds for all higher-order autocorrelation functions: for systems that are translational invariant in time, one time variable is usually eliminated [49] such that the kth-order correlation function only depends on $k-1$ time variables.

The Wiener-Chintchin theorem [1,50] relates the steady-state spin autocorrelation function to the noise power spectrum. It requires that the measuring time T_m is much longer that the characteristic time scale of the spin decay T^* ($T_m \gg T^*$). Substituting the Fourier transformation (15) and using the translational invariance in time, we obtain the second-order spin correlation function in the frequency domain:

$$\begin{aligned}\tilde{C}_2(\omega_1, \omega_2) &= \lim_{T_m \to \infty} \langle a(\omega_1) a(\omega_2) \rangle \\ &= \lim_{T_m \to \infty} \frac{1}{T_m} \int_{-\frac{T_m}{2}}^{\frac{T_m}{2}} dt_1\, e^{-\mathrm{i}\omega_1 t_1} \int_{-\frac{T_m}{2}}^{\frac{T_m}{2}} dt_2\, e^{-\mathrm{i}\omega_2 t_2} \\ &\quad \times \langle S_z(t_1) S_z(t_2) \rangle = \delta_{\omega_1, -\omega_2} C_2(\omega)\end{aligned} \tag{17}$$

with

$$C_2(\omega) = \int_{-\infty}^{\infty} d\tau\, \langle S_z(\tau) S_z(0) \rangle e^{-i\omega\tau}. \tag{18}$$

$C_2(\omega)$ denotes the spin-noise spectrum and satisfies the sum rule

$$\int_{-\infty}^{\infty} d\omega C_2(\omega) = \frac{\pi}{2}. \tag{19}$$

Note that the inclusion of the prefactor $1/\sqrt{T_m}$ into the definition of the Fourier transformation ensures the convergence of $\tilde{C}_2(\omega_1, \omega_2)$. It also leads to the Kronecker δ in the last line of Eq. (17) [51].

B. Fourth-order correlation function

While the second-order spin correlation has been extensively studied both in the frequency and the time domain [4,9,13], the properties of fourth-order correlation functions remain relatively unexplored [35].

An nth-order cumulant is given by the nth-order autocorrelation function from which all combinations of lower-order correlation functions are subtracted; see Ref. [39] for more details. The basic idea is to separate the true higher-order correlations from a trivial factorisation. If a system would be fully characterized by Gaussian noise, all higher-order cumulants would vanish [49].

One can show that the third-order spin correlation function is imaginary in the time domain and not accessible. In this paper, we therefore focus on the fourth-order spin correlation function. Its cumulant provides additional information on the dynamics of the system not yet included in C_2. The fourth-order cumulant of $a(\omega)$ is defined as

$$\begin{aligned}&\tilde{S}_4(\omega_1, \omega_2, \omega_3, \omega_4) \\ &\quad = \tilde{C}_4(\omega_1, \omega_2, \omega_3, \omega_4) - \tilde{C}_2(\omega_1, \omega_2)\tilde{C}_2(\omega_3, \omega_4) \\ &\qquad - \tilde{C}_2(\omega_1, \omega_3)\tilde{C}_2(\omega_2, \omega_4) - \tilde{C}_2(\omega_1, \omega_4)\tilde{C}_2(\omega_2, \omega_3),\end{aligned} \tag{20}$$

where we neglected the spin polarization in a finite magnetic field, which is justified in the high-temperature limit. The translational invariance in time in combination with the limit $T_m \gg T^*$ yields the constraint

$$\begin{aligned}\tilde{C}_4(\omega_1, \omega_2, \omega_3, \omega_4) = \delta_{\omega_1+\omega_2+\omega_3+\omega_4, 0} C_4[\omega_1, \omega_2, \omega_3, \\ -(\omega_1 + \omega_2 + \omega_3)].\end{aligned} \tag{21}$$

We are interested in a special case of the fourth-order cumulant $S_4(\omega_1, \omega_2) = \tilde{S}_4(\omega_1, -\omega_1, \omega_2, -\omega_2)$. Since $a(-\omega) = a^*(\omega)$, it correlates two spin-noise power spectrum components $|a(\omega)|^2$ at different frequencies with each other. Using Eq. (20), this bispectrum fulfils the relation

$$\begin{aligned}S_4(\omega_1, \omega_2) &= \tilde{S}_4(\omega_1, -\omega_1, \omega_2, -\omega_2) \\ &= C_4(\omega_1, \omega_2) - C_2(\omega_1) C_2(\omega_2) \\ &\quad \times (1 + \delta_{\omega_1, \omega_2} + \delta_{\omega_1, -\omega_2}).\end{aligned} \tag{22}$$

with $C_4(\omega_1, \omega_2) = \tilde{C}_4(\omega_1, -\omega_1, \omega_2, -\omega_2)$. In the limit $T_m \to \infty$, the last two terms in Eq. (20) are zero for $S_4(\omega_1, \omega_2)$ unless $\omega_1 = \pm\omega_2$.

If the two frequency components are uncorrelated, the fourth-order cumulant would vanish. If the cumulant features anticorrelation, i.e., $S_4(\omega_1, \omega_2) < 0$, the observation of a spin component with the frequency ω_1 decreases the likelihood of simultaneously observing a spin precession with the frequency ω_2.

In the long measurement limit, the Fourier transform of $C_4(\omega_1, \omega_2)$ becomes

$$C_4(t_1, t_2) = \frac{1}{T_m} \int_{-T_m/2}^{T_m/2} d\tau \langle S_z(t_1 + \tau) S_z(\tau) S_z(t_2) S_z \rangle. \tag{23}$$

This integrand describes the correlation of two $C_2(t_{1/2})$ measurements, one started at $t = 0$, the other started at τ. It is then averaged over the time delay between both measurements. This could be implemented in an experimental setup. It is similar, but not identical, to the fourth-order correlator $\langle S_z(t_1) S_z(t_1 + t_2) S_z(t_1) S_z \rangle$ [32,33]. We can therefore expect some comparable behavior, such as the sensitivity to quadrupolar interaction even at high magnetic fields.

It is straightforward to prove the sum rule

$$\int_{-\infty}^{\infty} d\omega_1 \int_{-\infty}^{\infty} d\omega_2 C_4(\omega_1, \omega_2) = \frac{\pi^2}{4} \tag{24}$$

from the definition of $C_4(\omega_1, \omega_2)$. Since the contributions to $S_4(\omega_1, \omega_2)$ containing $\delta_{\omega_1, \pm\omega_2}$ have the measure zero, the integral of $S_4(\omega_1, \omega_2)$ over the ω_1-ω_2 plane vanishes. This follows from the combination of Eqs. (19) and (24). Consequently, a nonvanishing bispectrum must contain as much spectral weight in the anticorrelations as in the correlations independently of the details of the Hamiltonian. Since the term $C_2(\omega_1) C_2(\omega_2)$ in Eq. (22) is well understood, the distribution of correlated and anticorrelated frequencies under the influence of a transversal magnetic field as well as quadrupolar interaction will be the focus of this paper.

IV. METHODS

In this section we discuss both the quantum-mechanical as well as the classical method employed for computing second and fourth-order correlation functions.

A. Quantum mechanical approach

Using an exact diagonalization of the Hamiltonian as a quantum-mechanical approach to the higher-order spin correlations suffers from the exponential growth of the Hilbert space $\mathcal{D} = \dim(H) = 2(2I + 1)^N$ with N, the number of nuclear spins. One can either utilize an approximate treatment of the dynamics or solve the problem exactly by fully diagonalizing the total Hamiltonian $H = H_{\mathrm{CSM}} + H_Q$. With this method the number of nuclear spins N is limited to a small bath size.

Diagonalizing the Hamiltonian $H_{\mathrm{CSM}} + H_Q$ produces a finite set of discrete eigenvalues and eigenvectors $H|n\rangle = E_n|n\rangle$. We use this eigenbase for calculating the spin-spin correlation function $C_2(\omega)$ in frequency space from Eq. (18)

$$C_2(\omega) = \frac{2\pi}{D} \sum_{nm} \delta(\omega - (E_n - E_m)) |S_{nm}|^2, \tag{25}$$

defining the spin operator matrix element $S_{nm} = \langle n|S_z|m\rangle$. The spin-noise spectrum $C_2(\omega)$ is positive semidefinite: the matrix elements $|S_{nm}|^2$ contribute if the excitation energy $E_n - E_m$ coincides with the external probe frequency ω.

The fourth-order spin correlation $C_4(\omega_1, \omega_2)$ can be expressed as

$$\begin{aligned} C_4(\omega_1, \omega_2) = \frac{4\pi^2}{D} \sum_{nml} \sum_{k \in U_n} &\delta(\omega_1 - (E_n - E_m)) \\ &\times \delta(\omega_2 - (E_k - E_l)) S_{nm} S_{mk} S_{kl} S_{ln}. \end{aligned} \tag{26}$$

U_n is the subspace of all eigenstates with the same eigenenergy E_n. If the Hamiltonian contains solely nondegenerate eigenstates, the sum over k reduces to a single term $k = n$:

$$\begin{aligned} C_4(\omega_1, \omega_2) = \frac{4\pi^2}{D} \sum_{nml} &\delta(\omega_1 - (E_n - E_m)) \\ &\times \delta(\omega_2 - (E_n - E_l)) |S_{nm}|^2 |S_{nl}|^2. \end{aligned} \tag{27}$$

While C_2 offers only information on the spin dynamics depending on one frequency, C_4 reveals the interplay between two frequencies, $\omega_1 = E_n - E_m$ and $\omega_2 = E_n - E_l$ weighed with the spin matrix element $|S_{nm}|^2$ and $|S_{nl}|^2$, respectively. Note that the δ functions in the Lehmann representations (25) and (26) imply the limit $T_m \to \infty$. For a finite measuring time $T_m < \infty$, the δ functions are broadened by a width $\propto 1/T_m$.

Combining Eqs. (25) and (26), the bispectrum $S_4(\omega_1, \omega_2)$ can be expressed as

$$\begin{aligned} S_4(\omega_1, \omega_2) = \frac{4\pi^2}{D} \Bigg\{ &\sum_{nml} \sum_{k \in U_n} [\delta(\omega_1 - (E_n - E_m)) \\ &\times \delta(\omega_2 - (E_k - E_l)) S_{nm} S_{mk} S_{kl} S_{ln}] \\ &- (1 + \delta_{\omega_1, \omega_2} + \delta_{\omega_1, -\omega_2}) \\ &\times \Bigg[\sum_{nm} \delta(\omega_1 - (E_n - E_m)) |S_{nm}|^2 \\ &\times \sum_{kl} \delta(\omega_2 - (E_k - E_l)) |S_{kl}|^2 \Bigg] \Bigg\}. \end{aligned} \tag{28}$$

B. Classical treatment

In the quantum-mechanical treatment, we used the definition of the operator $a(\omega)$ and performed the ensemble average by evaluating the trace over the Hilbert space. For the classical simulation we proceed in the same manner. There, the trace is replaced by a configuration average over all initial conditions [25,36]. The integral over the Bloch sphere of each spin is approximated by a finite number of randomly generated spin configurations. We track the time evolution $S_z(t)$ determined by Eq. (10) in each configuration.

For the case of $\omega_1 = -\omega_2$ and $\omega_4 = -\omega_3$, the correlation function $\tilde{C}_4(\omega_1, \omega_2, \omega_3, \omega_4)$ can be written as

$$C_4(\omega_1, \omega_2) = \frac{1}{N_C} \sum_{i \in \mathrm{config}} \mathcal{F} C_2^i(\omega_1) \mathcal{F} C_2^i(\omega_2). \tag{29}$$

In each classical configuration i, the Fourier transformation of the electron spin correlation $C_2^i(t) = S_z^i(0) S_z^i(t)$ provides building blocks for the correlation between the frequencies ω_1 and ω_2.

The correlation function $C_2(\omega_1)$ [29,46] that is subtracted from the fourth-order correlator in the cumulant S_4, cf.

Eq. (28), is calculated using

$$C_2(\omega_1) = \frac{1}{N_C} \sum_{i \in \text{config}} \mathcal{F} C_2^i(\omega_1). \tag{30}$$

While $C_2(\omega_1)$ contains $1/3$ of its total spectral weight at low frequencies $\omega \ll \omega_{\text{fluc}}$ at $b_{\text{ext}} = 0$ [14,15,29], it becomes Gaussian for $b_{\text{ext}} \gg T^* \omega_{\text{fluc}}$. The bispectrum $S_4(\omega_1, \omega_2)$ is then computed via Eq. (22), analogous to the quantum-mechanical method.

V. RESULTS

A. Choice of parameters

For the simulation, physical realities need to be translated into parameters for the model to best reflect the actual system. While the number of nuclei in a quantum dot is of the order of 10^4–10^6, simulating them all is computationally nonviable. In modeling the hyperfine interaction between electron and nuclei, we, therefore, neglect all nuclei whose distance from the electron exceeds a cutoff radius R_0. Following from Eq. (8), the resulting distribution of hyperfine coupling constants in a QD of the radius L_0 is realized by

$$A_k = A_{\max} \exp\left(- r_0^m \beta^{m/d} \right) \tag{31}$$

with $r_0 = R_0/L_0$ and β randomly selected from a uniform distribution, $\beta \sim \mathcal{U}(0,1)$. Then the set $\{A_k\}$ is properly normalized such that they always yield the same ω_{fluc} defined in Eq. (2). The distribution of Eq. (31) was already applied in the Refs. [13–16].

To generate an adequate representation of the a_k distribution, it is necessary to adjust the cutoff radius depending on the bath size to prevent the dynamics being dominated by only a few strongly coupled nuclear spins. For small baths ($N < 15$) we choose the relative cut-off radius $r_0 = 0.8$, while a larger cutoff $r_0 = 1.5$ is utilized for large baths. Here, a ($d = 3$)-dimensional quantum dot with a Gaussian electron wave envelope, $m = 2$, is studied. To gauge the influence of quadrupolar couplings on the decay without having to account for the decay due to the hyperfine coupling distribution, homogeneous couplings ($A_k = \text{const}$, $R_0 = 0$) are used as well.

We average over the Zeeman energies of the isotopes making up an InGaAs QD to estimate the ratio between nuclear and electron Zeeman energy, ζ. This results in $\zeta = 1/800$; the nuclear Zeeman splitting is about three orders of magnitude smaller than the electron Zeeman splitting and perturbative for dimensionless magnetic fields $\vec{b}_{\text{ext}}$ smaller than $O(10^2)$.

To quantify the relative quadrupolar interaction, we introduce the dimensionless ratio [13]

$$Q_r = \frac{\sum_k q_k}{\sum_k A_k}, \tag{32}$$

which relates the total quadrupolar interaction strength to the hyperfine coupling strength.

First, a set $\{\tilde{q}_k\}$ is obtained from a uniform distribution $\tilde{q}_k \in [0.5, 1]$. With a given Q_r, the quadrupolar interaction constants q_k are determined via

$$q_k = Q_r \tilde{q}_k \frac{\sum_k A_k}{\sum_k \tilde{q}_k} \tag{33}$$

to satisfy the relation in Eq. (32). The local easy axes $\vec{n}_k$ [48] have been reproduced by generating isotropically distributed vectors and discarding any vector at an angle with the growth axis larger than $\theta_{\max} = 34°$, so that the mean angle becomes $\overline{\theta} = 23°$. The z axis is aligned to the growth axis of the QD, while the external magnetic field is applied transversally, $\vec{b}_{\text{ext}} = b_x \vec{e}_x$ unless otherwise stated.

The δ distributions in Eq. (28) are represented by Lorentzians

$$\Gamma(\omega, \Delta E) = \frac{1}{\pi} \frac{\gamma}{(\omega - \Delta E)^2 + \gamma^2} \tag{34}$$

with a broadening factor $T^*\gamma = 0.01$. This broadening corresponds to a measuring time $T_m = 100\, T^*$. Although, the choice of this rather arbitrary broadening factor influences the magnitude of $S_4(\omega_1, \omega_2)$, the total spectral weight remains invariant of the broadening.

In an hypothetical quantum-mechanical simulation with 10^5 nuclear spins, the excitation spectrum entering Eqs. (25) and (26) will be dense due to the almost continuous distribution of the hyperfine couplings A_k in such a large spin ensemble. In a very small representation of the nuclear spin bath, the excitation energies become visibly discrete, and the number of different frequencies are further reduced by the degeneracies in the absence of an external magnetic field. In order to compensate for this effect, we generate N_a different sets of $\{A_k\}$, perform independent exact diagonalizations leading to a variation of the excitation spectrum [14] and average over the individual spectral functions. In the limit $N_a \to \infty$ the excitation spectrum should approach a continuum, at a finite N_a, the Lorentzians (34) start to overlap resulting in smoothed spectra. We set $N_a = 32$ providing a reasonable compromise between the computational effort and the smoothness of the spectra.

To obtain the equivalent between the quantum-mechanical expectation value and the classical simulation, the averaging over N_C classical initial spin configurations is necessary. $N_C = 10^5$ is considered a sufficiently large number of configurations to adequately represent the entirety of the sample space of the spins. Each configuration comprises $N = 100$ randomly generated nuclear spins and a central spin that is fully aligned in z direction at $t = 0$.

In the simulation all classical spin vectors are of length unity [25]. This necessitates the adjustment of the hyperfine coupling constants $a'_k = S a_k$ and of the Overhauser field $\vec{b}'_{\text{N}} = I/S \vec{b}_{\text{N}}$. It also translates to the quadrupolar interaction $q'_k = I q_k$. The classical spin always represents an effective spin vector length of $S = I = 1/2$ for simplicity.

B. Spin-noise power spectrum $C_2(\omega)$

To set the stage for higher-order spin correlation functions, we revisit the second-order spin noise $C_2(\omega)$ first. A basic understanding of spin noise was achieved when using the Fourier transform of the frozen Overhauser field approximation (FOA) [29]. The spin-noise spectrum was extracted analytically for $b_x = 0$ and numerically calculated for arbitrary magnetic fields. It was amply discussed in Refs. [10,13–15]. In Fig. 1 we provide a comparison of our two methods with this analytic approximation. The quantum-mechanical and the

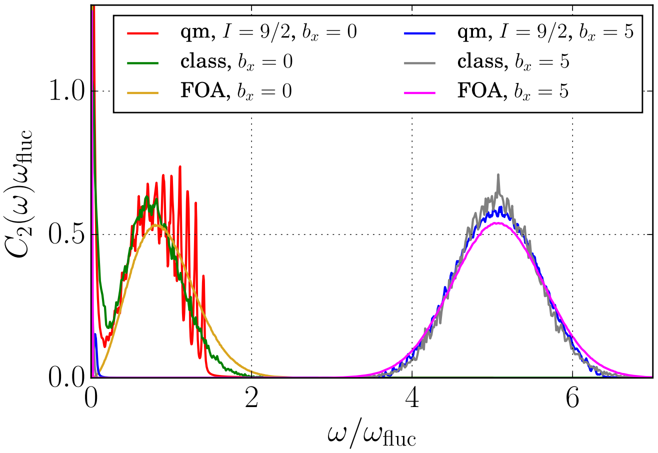

FIG. 1. Comparison between the spin noise $C_2(\omega)$ for different approaches: blue and red lines represent the quantum-mechanical simulation with three $I = 9/2$ nuclear spins, the green and grey lines are a classical simulation and the dark yellow and magenta lines are calculated from a Fourier transformed FOA.

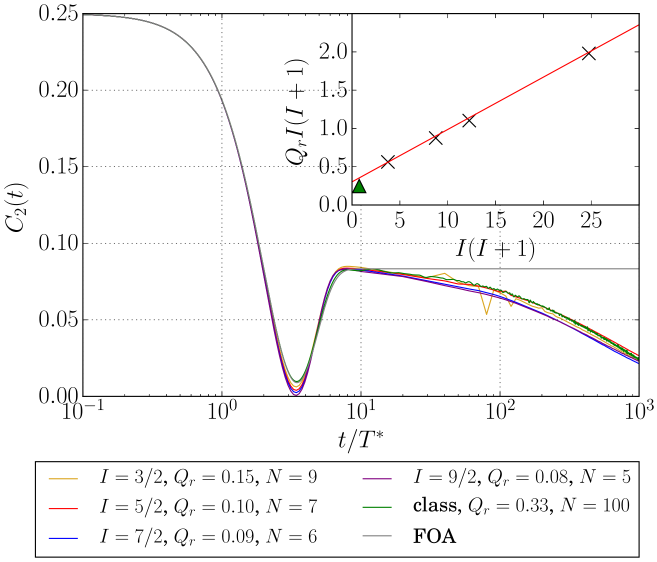

FIG. 2. $C_2(t)$ in the absence of an magnetic field computed by a Lanczos algorithm, with different spin lengths I, bath sizes N, and interaction strengths Q_r, chosen for similar long-time decay. The inset plot shows the dependence of $Q_r I(I+1)$ on the squared spin length $I(I+1)$. The hyperfine couplings are homogeneous. The analytical result of $C_2(t)$ obtained by the FOA is plotted in gray for comparison.

classical simulations show good agreement with the solution of the FOA for $b_x = 5$. The deviations of the quantum-mechanical result are related to the small number of simulated bath spins. At $b_x = 0$, the full spin rotational invariance introduces degeneracies in the eigenenergies leading to a reduction of the excitation spectrum. Therefore, the $N_a = 32$ different sets of hyperfine coupling constants are insufficient, and the distinct nuclear frequency peaks are visible in the spectrum. This is substantially different at finite $b_x = 5$ where these degeneracies are lifted by the Zeeman splitting, leading to an almost smooth spectrum. The classical simulation traces the Gaussian envelope of the quantum-mechanical spectrum and also differs from the FOA at $b_x = 0$. This is due to the nuclear spin dynamics included in Eq. (11) that causes an additional long-time decay in the time domain not included in the FOA. Therefore, spectral weight shifts from the δ peak at $\omega = 0$ to the Gaussian as the nondecaying fraction of $\langle S_z(t)S_z(0)\rangle$ decreases.

When adding the quadrupolar coupling to the central spin model, it is important to understand its influence on the long-time decay of $C_2(t)$ as a function of the bath spin length as well as number of nuclear spins in the simulation. The relative strength Q_r defined in Eq. (32) has been originally introduced in Ref. [15] to minimize this dependency. Since there is clear experimental evidence [15,32] that H_Q induces a second long-time decay of $C_2(t)$, which occurs on time scales of 200–600 ns depending on the growth conditions of the quantum dot ensemble, we aim for adjusting the value of Q_r for each simulation such that $C_2(t)$ remains invariant under the change of the bath size or the spin length in order to maintain a close connection between our simulations and the experiments. By establishing this gauge we are able to compare the differences in the fourth-order spectra with different bath spin lengths I as well as to link the quantum and the classical simulation.

Figure 2 depicts the second-order correlation function $C_2(t)$ for different I but similar Hilbert space dimensions $\mathcal{D}$, with a different but properly adjusted Q_r. In order to have a well-defined reference spectra that converges rapidly to an analytically known result in the limit of $N \to \infty$ [29], we chose homogeneous coupling constants $A_k = \text{const}$. In this case, all nuclear spins precess with an identical Knight field around the central spin at each given moment in time. By transforming the system into the rest frame of the total spin the problem becomes identical to the FOA added as a gray reference curve. The short-time dephasing occurs on the time scale T^*. The quantum-mechanical simulation tracks the FOA for infinity large bath sizes and rapidly converges to the FOA for short time scales. The data of the classical simulation for $N = 100$ cannot be distinguished from the FOA and differ only by the statistical fluctuation, which are not resolvable in Fig. 2. The spin symmetry in the CSM leads to a nondecaying fraction of $C_2(0)/3$ in the long-time limit [10,29] for $Q_r = 0$. A finite Q_r breaks this spin symmetry and introduce an additional secondary decay of the nondecaying fraction of $C_2(t)$ on a time scale $T_2 \gg T^*$ determined by the quadrupolar interaction strength [13,15,52].

We adjusted Q_r for the different parameters using for the plots in Fig. 2 in such a way that the long-time decay of all $C_2(t)$ is characterized by the same long-time scale T_2. By choosing homogeneous coupling constants A_k we can ensure that the long-time decay, $T^* < t$, is entirely controlled by the quadrupolar coupling.

For $I = 3/2$, the quadrupolar coupling strength is set to $Q_r = 0.15$, since this value has been successfully used to model experimental data [15,33]. Q_r were chosen for $I = 5/2$, $7/2$ and $9/2$ (marked by X in the inset of Fig. 2) so that all correlation functions exhibit a similar long-time decay. Interestingly, the Q_r that achieve this agreement of $C_2(t)$ for

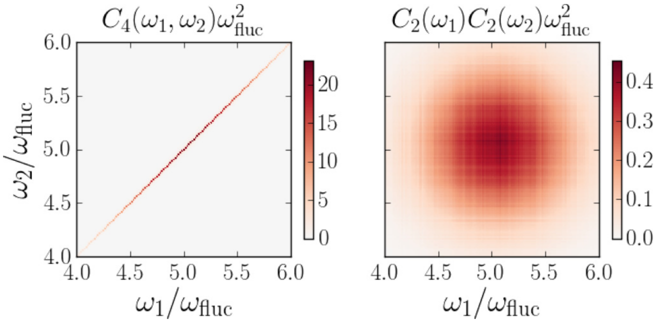

FIG. 3. $C_4(\omega_1,\omega_2)$ and $C_2(\omega_1)C_2(\omega_2)$ as the result of a classical simulation. The cumulate S_4 spectrum is shown in Fig. 7. The external magnetic field is $b_x = 5$.

these different combinations of I and N obey the relation

$$Q_r I(I+1) = aI(I+1) + b, \tag{35}$$

with $a = 0.068 \pm 0.002$ and $b = 0.30 \pm 0.03$ obtained via linear regression. The classical computations of $C_2(t)$ that have been made for an effective spin vector length of $I = 1/2$ follow this relation roughly (marked by a triangle in the inset plot).

C. Fourth-order spin noise in the CSM

A comparison of the quantum-mechanical and classical simulation results for the fundamental features of the fourth-order cumulant S_4 is the topic of this section. We discuss how the shape of S_4 is determined by its components C_4 and C_2 as well as the dependence of the spectrum on $\vec{b}_{\rm ext}$. The classical simulation is presented as a limiting case to the quantum-mechanical calculation. To set the stage we limit ourselves for now to the CSM, which excludes the quadrupolar interaction.

1. Components of S_4 depending on external magnetic field strength

Each S_4 spectrum consists of two parts: $C_4(\omega_1,\omega_2)$ and the product $C_2(\omega_1)C_2(\omega_2)$, cf. Eq. (28). The results of the classical simulation for $b_x = 5$ are depicted in Fig. 3. Since both terms only contain quadratic expressions, their individual contributions are positive.

$C_2(\omega)$ is to good approximation a Gaussian with the mean given by $\sqrt{b_x^2 + 1/2}$, cf. [14], and its variance σ^2 is determined by the Fourier transform of the envelope of the central spin dynamics in the time domain for large magnetic fields $(\omega_{\rm fluc}/2)^2$ [29]. Since ω_1 and ω_2 are independent variables, the covariance is the identity matrix in the multivariate Gaussian given by $C_2(\omega_1)C_2(\omega_2)$ as shown in the right panel of Fig. 3.

$C_4(\omega_1,\omega_2)$ is plotted in the left panel of Fig. 3. It only contributes on the diagonal $\omega_1 = \omega_2$. This fact is intuitively accessible in the classical approach. In each configuration the hyperfine interaction changes the initial frequency given by the generated Overhauser field only marginally. Therefore, the Fourier transform of $C_2^i(t)$ can be described by a narrow peak and the product of two distributions can only be nonzero at the overlap. For better visibility the δ peaks are broadened to a Lorentzian with a width of $\gamma T^* = 0.01$. In the direction of the diagonal, the spectrum follows a Gaussian distribution $\mathcal{N}(\sqrt{b_x^2 + 1/2}, (\omega_{\rm fluc}/2)^2)$. This agrees with the result of FOA [29], since a high magnetic field suppresses spin flips, leading to an Ising model and which features a Gaussian distribution of polarization due to the central limit theorem.

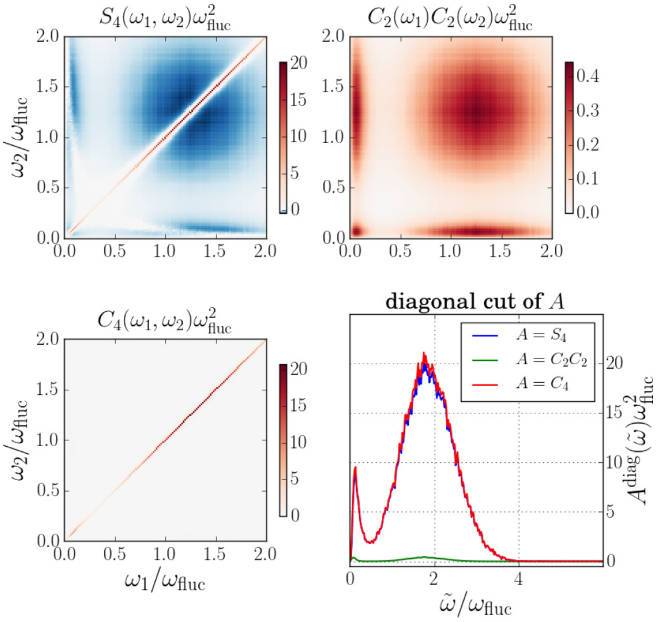

FIG. 4. $S_4(\omega_1,\omega_2)\omega_{\rm fluc}^2$ as well as $C_4(\omega_1,\omega_2)\omega_{\rm fluc}^2$ and $C_2(\omega_1)C_2(\omega_2)\omega_{\rm fluc}^2$ for $b_x = 1$ in the classical simulation with $N = 100$ bath spins. In the bottom right panel the diagonal cut through all three spectra is shown.

Combining the two contributions $C_4(\omega_1,\omega_2)$ and $C_2(\omega)$ leads to dominating correlations on the diagonal $\omega_1 = \omega_2$ as well as anticorrelations elsewhere in the (ω_1,ω_2)-plane as a consequence of the subtraction of both terms in Eq. (22).

To parametrize the diagonal cut we define $S_4^{\rm diag}(\tilde{\omega}) = S_4(\tilde{\omega}/\sqrt{2}, \tilde{\omega}/\sqrt{2})$ and plot $S_4^{\rm diag}(\tilde{\omega})$ in the bottom right panel of Fig. 4. For small magnetic fields the spectrum changes distinctively, as can be seen in Fig. 4. Again we find a Gaussian centered around $\sqrt{b_x^2 + 1/2}$ with a variance of $(\omega_{\rm fluc}/2)^2$ but with reduced spectral weight. For $b_x = 0$ the correlator C_2 features a strongly pronounced δ peak at $(\omega_1,\omega_2) = (0,0)$, as seen in Fig. 1, with a maximum weight of one third of the total spectral weight in the case of homogeneous coupling constants [29]. Increasing the strength of the external magnetic field not only shifts the position of the Gaussian depending on the external magnetic field but also transfers the weight of the δ peak to the Gaussian. For higher magnetic fields, e. g., $b_x = 5$, the contribution at (0,0) has vanished, and only the Gaussian remains. The same behavior also influences the C_4 part of the spectrum, where we can observe a not yet disappeared δ peak at the origin of coordinates for $b_x = 1$.

After establishing the qualitative features of C_4 as well as the product C_2C_2 for smaller and intermediate transversal field strength b_x by the classical simulation, we compare these results with the quantum-mechanical calculations for a very small bath but with large nuclear in $I = 9/2$ along the diagonal $\omega_1 = \omega_2$.

$S_4^{\rm diag}(\tilde{\omega})$ for high magnetic fields is shown in Fig. 5. The definition can be used analogously for the diagonal cuts

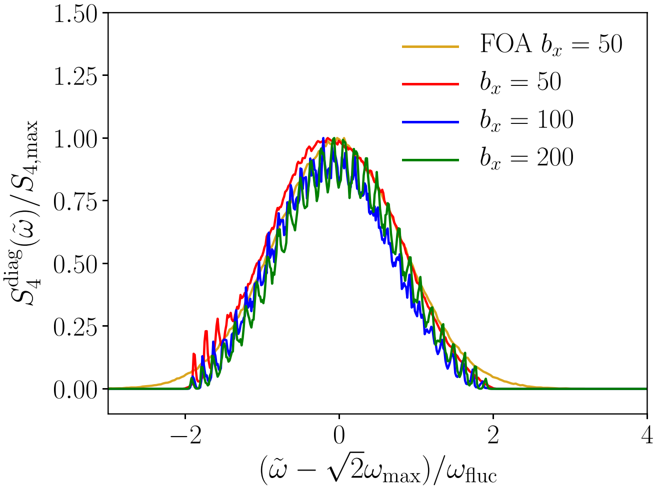

FIG. 5. $S_4^{\mathrm{diag}}(\tilde{\omega})$ for high ($b_x = 50, 100, 200$) transversal magnetic fields. Computed via the quantum-mechanical scheme for $N = 3$ bath spins with a spin length of $I = 9/2$. The spectra are shifted by $\sqrt{2}\omega_{\mathrm{max}} = \sqrt{2}\sqrt{b_x^2 + 1/2}$. The frozen Overhauser field approximation (FOA) is included for comparison.

through the $C_2(\omega_1)C_2(\omega_2)$ and $C_4(\omega_1, \omega_2)$ spectra. While the quantum-mechanical spectra is centered around $\sqrt{b_x^2 + 1/2}$ at all magnetic fields and is tracing the Gaussian envelope established in the classical simulation for smaller fields, it develops a comb of peaks at high magnetic fields. At larger fields, spin-flip processes are suppressed, and the dynamics becomes increasingly dominated by the Ising part of the CSM in x direction. The peak location is governed by the hyperfine interaction, with the distance decreasing with increasing bath sizes, $\propto 1/\sqrt{N}$. The width of the peaks relates to the variability of the A_k. This phenomenon can not be observed with a classical computation, where higher magnetic fields only shift the spectrum which maintains its continuous shape. With higher numbers of bath spins and a distribution of A_k with high variability, the quantum-mechanical spectrum would approach the results of the classical simulation.

2. Classical simulation as a limiting case of the quantum-mechanical treatment of S_4

While the classical approach always yields a continuous frequency spectrum, the variation of nuclear spin length as well as the bath size merits a more in-depth investigation for the quantum-mechanical simulation. Figure 6 shows the quantum-mechanical results for $S_4(\omega_1, \omega_2)$ obtained by Eq. (28) for different spin lengths ($I = 3/2,\ 5/2,\ 7/2$) and a fixed number of bath spins ($N = 3$) in a transversal field $b_x = 5$ applying an average over $N_a = 32$ configurations of $\{A_k\}$. The spectrum becomes more continuous with a growing spin length, due to the exponential increase in the Hilbert space dimension and the larger number of nondegenerate eigenenergies. As seen in the left panel of Fig. 6, the nonzero contributions to S_4 are concentrated at a sparse number of (ω_1, ω_2) frequency pairs for $N = 3 I = 3/2$-spins, due to the limitations of the energy excitation spectrum. The δ peaks in Eq. (28) are broadened by a factor $\gamma T^* = 0.01$. Correlations (red) are restricted to the frequency subspace $\omega_1 = \omega_2$, while the anti-correlations (blue) can be found in an area centered around $\omega_1 = \omega_2 \approx b_x$. Note the similarity between the classical results (Fig. 7, bottom right panel) and the quantum-mechanical solution for $N = 3$ and $I = 7/2$ (Fig. 6, right panel), solidifying the conjecture that the quantum-mechanical spectra approaches the results of the classical simulation in the limit of $I \to \infty$.

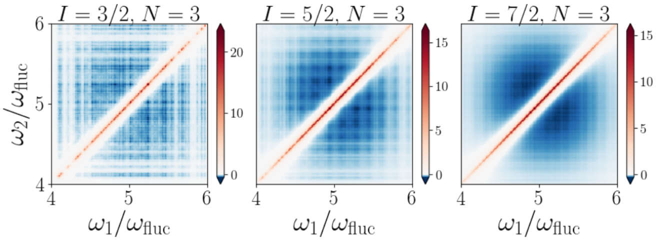

FIG. 6. $S_4(\omega_1, \omega_2)$ computed for a bath size of $N = 3$ with spin lengths $I = 3/2$, $I = 5/2$, and $I = 7/2$ and an A_k configuration with $r_0 = 0.8$. The transversal magnetic field is set to $b_x = 5$, and quadrupolar interaction is switched off.

The fourth-order cumulant spectra $S_4(\omega_1, \omega_2)$ are presented for different N and a fixed spin length $I = 9/2$ at $b_x = 5$ in Fig. 7. For $N = 1$, the position of the nonzero contributions are clearly governed by the Zeeman splitting of the nuclear spins coupled to the central spin via a single hyperfine coupling constant $A = \omega_{\mathrm{fluc}}$. This results in $(2I + 1)^2$ equidistant peaks on a grid around the point given by (ω_L, ω_L), that are positive at the $\omega_1 = \omega_2$ diagonal and negative everywhere else. For larger bath sizes the spectrum becomes more continuous. At $N = 3$ bath spins of length $I = 9/2$ the S_4 spectrum, as displayed in the bottom left panel of Fig. 7, is already qualitatively very similar to the classical result depicted on the bottom right panel of Fig. 7.

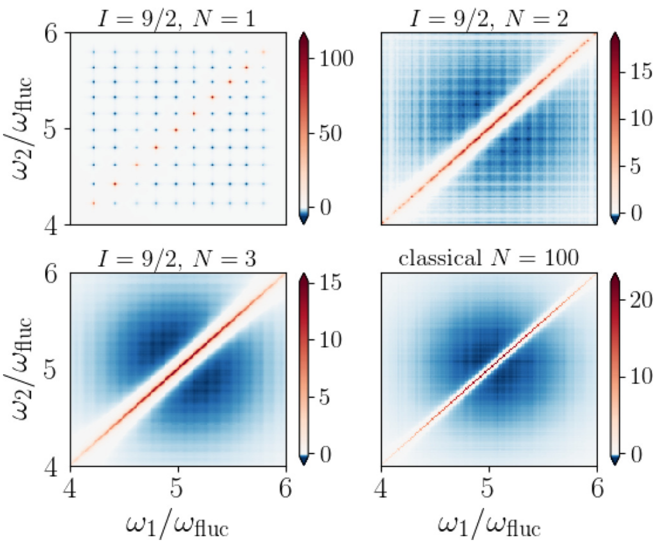

FIG. 7. $S_4(\omega_1, \omega_2)$ computed for $N = 1, 2, 3$ bath spins with $I = 9/2$, and for $N = 100$ classical spins. The transversal magnetic field is $b_x = 5$, and quadrupolar interaction is not included.

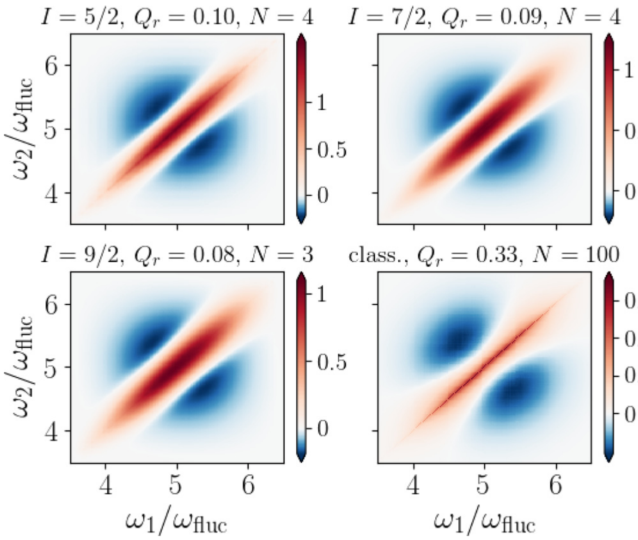

FIG. 8. $S_4/\omega_1, \omega_2)$ with a magnetic field $b_x = 5$, with different spin lengths I, bath sizes N, and interaction strengths Q_r. The parameters are chosen for similar behavior in the second-order spin correlation, see Fig. 2.

The simulations show that the classical calculations are valid limits of the quantum-mechanical calculations for $I \to \infty$ and $N \to \infty$. Furthermore, we established that fourth-order cumulant does not vanish implying that the central spin does not behave as a classical random variable whose noise spectrum is purely of Gaussian type. The physics is driven by the coherent precession around the external constant magnetic field in combination with a slowly varying nuclear spin dynamics. The FOA reveals the restriction of C_4 to the frequency diagonal, which is shared by both approaches that explicitly include the nuclear spin dynamics.

D. Influence of quadrupolar interaction on $S_4(\omega_1, \omega_2)$

Within the CSM, the positive correlations are restricted to the diagonal $\omega_1 = \omega_2$ related to the spectral confinement of $C_4(\omega_1, \omega_2)$ leading to anticorrelation everywhere else in the frequency plane. In this section, we add the nuclear-electric quadrupolar interaction H_Q to the CSM and investigate its influence onto S_4.

1. Fourth-order spin noise at intermediate and large magnet fields

Here, we focus on intermediate and large magnet fields since in this regime the spin-noise power spectrum $C_2(\omega)$ remains unaltered in the presence of quadrupolar interaction. In leading order $C_2(\omega)$ is described by a Gaussian [29,46] centered around ω_1; see also Sec. V B.

Figure 8 shows $S_4(\omega_1, \omega_2)$ computed quantum mechanically for bath spin lengths $I = 3/2,\ 7/2,\ 9/2$ as well as the results of the classical approach. The strength of the quadrupolar coupling is chosen such that $C_2(t)$ agrees for $b_{\rm ext} = 0$ independent of the spin length; see the discussion in Sec. V B. While the fourth-order contribution to S_4 is restricted to the diagonal, $\omega_1 = \omega_2$ without quadrupolar interaction, the introduction of quadrupolar couplings causes a broadening of the heretofore sharp peak. But while the quantum-mechanical cumulant spectra look very similar, the classically computed S_4 exhibits a much smaller broadening of the positive contribution around $\omega_1 = \omega_2$, and a qualitatively different peak shape as can be seen in the bottom right panel of Fig. 8. Since the quadrupolar interaction does not affect the shape of $C_2(\omega)$ for transversal magnetic fields $b_x > 1$ in both approaches, the mismatch between quantum-mechanical and classical fourth-order cumulant is related to C_4.

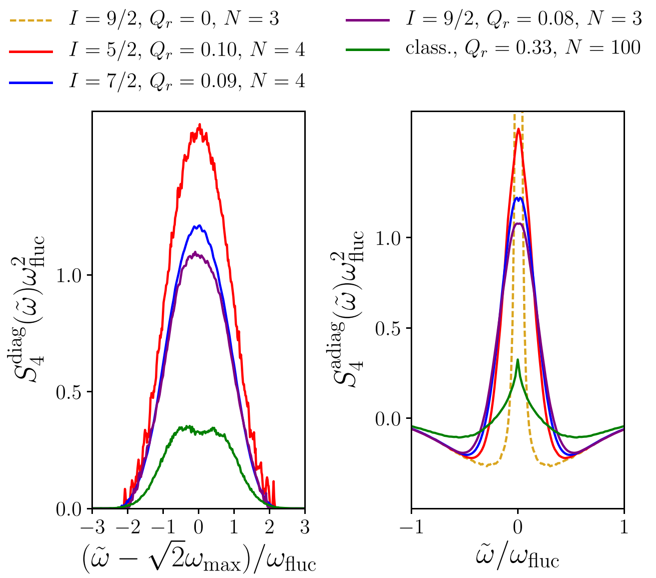

FIG. 9. The same data plotted in Fig. 8, cut in the diagonal $\omega_1 = \omega_2$, $S_4^{\rm diag}(\tilde\omega)$, as well as in the antidiagonal cut $\omega_1 + \omega_2 = 2\omega_{\rm max}$, $S_4^{\rm adiag}(\tilde\omega)$. $S_4^{\rm diag}(\tilde\omega)$ without quadrupolar coupling was added in the right panel for comparison.

To quantify the influence of the quadrupolar coupling strength Q_r onto the cumulant S_4, we analyze the broadening of C_4 perpendicular to the frequency diagonal. For that purpose, we parametrize the antidiagonal cut in the vicinity of its global maximum, $S_4(\omega_{\rm max}, \omega_{\rm max})$, with $\omega_{\rm max}/\omega_{\rm fluc} = \sqrt{b_x^2 + 1/2}$ by $\omega_1 + \omega_2 = 2\omega_{\rm max}$. We define the corresponding antidiagonal cut as

$$S_4^{\rm adiag}(\tilde\omega) = S_4\left(\omega_{\rm max} + \frac{\tilde\omega}{\sqrt{2}}, \omega_{\rm max} - \frac{\tilde\omega}{\sqrt{2}}\right) \qquad (36)$$

so that the global maximum is located at the relative frequency $\tilde\omega = 0$.

The diagonal and antidiagonal cuts of the data presented in Fig. 8 are plotted in Fig. 9. The same parameters that produced congruent results for conventional spin-noise spectrum $C_2(\omega)$ as shown in Fig. 1, now lead to markedly different behavior. The left panel shows the diagonal cuts computed with the quantum-mechanical method for different nuclear spin length I and bath size N and is augmented by the results of the classical approach for $N = 100$ nuclear spins. The diagonal cuts exhibit roughly the same Gaussian behavior independent of Q_r, but its amplitude decreases by about a factor five. This is a direct result of the broadening observed in Fig. 8, as the total spectral weight of C_4 as well as S_4 remains conserved. The drop in amplitude is not uniform, but is more pronounced

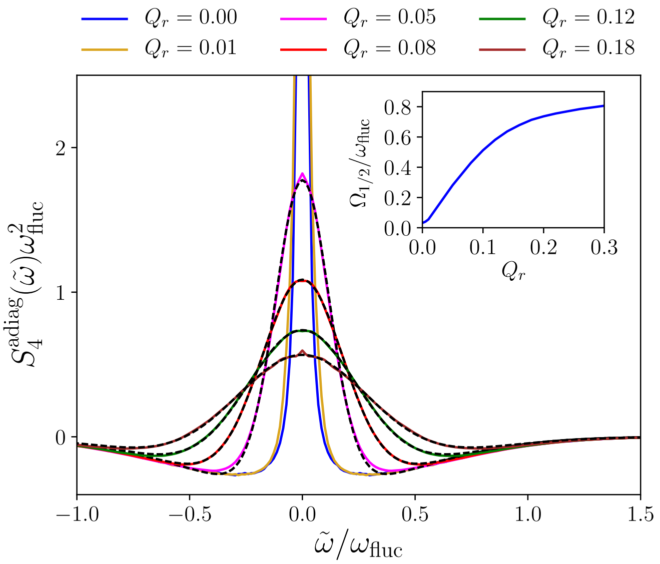

FIG. 10. $S_4^{\rm adiag}(\tilde\omega)$ quantum mechanically calculated with $N = 3$, $b_x = 5$, and $I = 9/2$ for different Q_r. The inset plot shows the full width half maximum $\Omega_{1/2}$ of C_4 in relation to the quadrupolar coupling strength Q_r.

in S_4 computed via the classical approach, suggesting that the quadrupolar coupling has a stronger effect there. In the quantum mechanically computed S_4 the amplitude decreases with larger I.

On the right panel of Fig. 9 the antidiagonal cuts are shown for the same parameters as in the left panel. Added for comparison is $S_4^{\rm adiag}(\tilde\omega)$ for $Q_r = 0$ obtained with the same broadening parameter γ. $S_4^{\rm adiag}(\tilde\omega)$ reveals a fundamentally different curve shape depending on the computational approach. While the classical curve exhibits a cusp, which could be fitted by a power law, the quantum-mechanical approach yields a Gaussian shape.

The scaling behavior, which allows us to match classical and quantum mechanical results for $C_2(\omega)$ by adjusting Q_r, cf. Sec. V B, therefore only holds for the second-order spin noise and not the fourth-order spin-noise bispectrum. It stands to reason that the quantum-mechanical method includes features that have been neglected in the classical approach, such as the noncommutability of the bath spin components.

In order to connect the relative quadrupolar coupling strength Q_r with the broadening of the antidiagonal, we plotted $S_4^{\rm adiag}(\tilde\omega)$ for different Q_r and fixed $N = 3$ and $I = 9/2$ in Fig. 10. The contribution $C_2(\omega_1)C_2(\omega_2)$, can be represented by a Gaussian with the variance $\sigma^2 = (\omega_{\rm fluc}/2)^2$ independent of Q_r compatible with the FOA [29]. The fourth-order contribution C_4 in contrast changes markedly with the quadrupolar interaction strength. Fitting only C_4 with a Gaussian leads to the relation between the full width half maximum $\Omega_{1/2}$ and the quadrupolar coupling strength Q_r shown in the inset of Fig. 10. For small Q_r, the dependence is roughly linear, before the increase flattens at $Q_r > 0.1$. For $Q_r \to 0$, the Gaussian curve becomes a sharp peak $\Omega_{1/2} \to 0$ limited here due to the Lorentz broadening simulating a finite measuring time T_m.

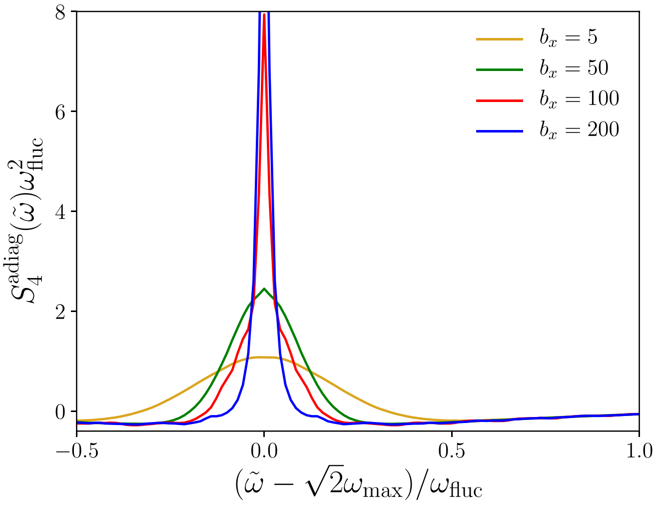

FIG. 11. $S_4^{\rm adiag}(\tilde\omega)$ quantum mechanically calculated with $N = 3$, $Q_r = 0.08$, and $I = 9/2$ for different transversally applied external magnetic fields b_x.

Figure 11 depicts the antidiagonal cut $S_4^{\rm adiag}(\tilde\omega)$ for different magnetic fields b_x and fixed spin bath size and spin length. The quadrupolar coupling induced broadening decreases with an increasing magnetic field strength: the dynamics of the system is dominated by the Zeeman energy, and H_Q becomes an increasingly weaker perturbation. This agrees well with the observation of the fourth-order spin correlation function in the time domain [33], where the high magnetic fields shift the decay time from O(ns) to an exponential decay with a magnetic-field-dependent decay time $T_2 \propto O(\mu{\rm s})$ [9,31,32].

We performed the same type of simulations as in Fig. 10 using the classical approach. Figure 12 shows $S_4^{\rm adiag}(\tilde\omega)$ for different Q_r. Since $C_2(\omega)$ remains invariant under the change of Q_r, the change in the spectrum is directly linked to the change of $C_4(\omega_1, \omega_2)$. As in the quantum-mechanical simulations, the quadrupolar interaction lifts the spectral constrain to $\omega_1 = \omega_2$ in $C_4(\omega_1, \omega_2)$. The overall sum-rule for $C_4(\omega_1, \omega_2)$

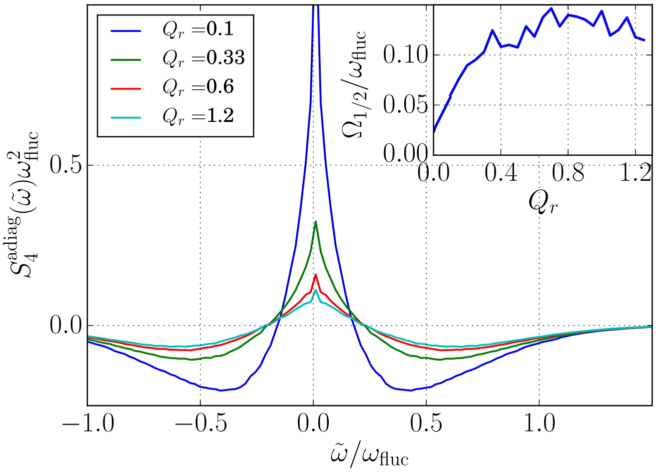

FIG. 12. Cuts for the classically calculated $S_4^{\rm adiag}(\tilde\omega)$. The inset plot shows the full width at half maximum $\Omega_{1/2}$ of the C_4 part dependent on the quadrupolar coupling strength Q_r.

implies a decrease of the peak at $\tilde{\omega} = 0$ and an increasing distribution of spectral weight into the (ω_1, ω_2) plane. Since the shape of the classical $S_4^{\text{adiag}}(\tilde{\omega})$ is non-Gaussian, we extracted the full width half maximum $\Omega_{1/2}$ of C_4 as function of Q_r and plotted the result as inset in Fig. 12. In full agreement with the quantum-mechanical approach we find a linear dependency of $\Omega_{1/2}$ on Q_r for small $Q_r < 0.35$. The finite offset at $Q_r = 0$ is related to the finite size effect of the Fourier transformation for $T_m < \infty$. The absolute value of $\Omega_{1/2}$, however, differs between the quantum-mechanical and the classical simulations, which we attribute to the bath size difference. For larger quadrupolar interaction strength the width $\Omega_{1/2}$ does not increase further. This agrees qualitatively with the quantum-mechanical simulation where the full width half maximum also flattens out. As an upper bound we assume $\Omega_{1/2}/\omega_{\text{fluc}} = 0.147$ which was measured at $Q_r = 0.7$.

But most importantly the shape of $S_4^{\text{adiag}}(\tilde{\omega})$ is deformed from an approximately exponential shape to a Gaussian with a peak at the mean value. A similar behavior can be observed in the quantum-mechanical simulation for the external magnetic field dependency with fixed Q_r as depicted in Fig. 11. The increase of the external magnetic field goes together with the change of the broadening at $b_x = 100$ and its final exponential shape at $b_x = 200$.

The approach of a constant $\Omega_{1/2}$ for larger values of Q_r can be understood by inspecting the dynamics of an isolated nuclear spin that is determined by two energy scales: the Zeeman energy and the quadrupolar coupling. For small magnetic fields the quadrupolar coupling leads to energy separated time-reversal pairs of doublets that are only weakly perturbed. In this limit, an increasing quadrupolar coupling linearly widens the energy separation between these time-reversal pairs: spin-flip scattering processes between different doublets are suppressed. Consequently the central spin dynamics becomes independent of Q_r once the quadrupolar interaction considerably exceeds the Zeeman energy leading to a constant $\Omega_{1/2}$ for larger values of Q_r. For a very large Zeeman energy the quadrupolar interaction can be seen as weak perturbation; the crossover happens when the energy scales are comparable. In the large field limit, the effect of the quadrupolar interaction is suppressed again leading to a narrowing of the spectra in Fig. 11 as already discussed above.

In a real system, the individual values of q_k are dependent on the local strain tensor that is not explicitly known in detail. In the numerical simulation the parameter Q_r was fixed by connecting the simulated second-order spin correlation function with the corresponding experiments [13,31,32]. However, for a specific nuclear spin in the simulation the ratio between the Zeeman energy and q_k does not only depend on the distribution of the strain fields but also on the average value of q_k that remains N dependent. Since the classical simulation involves more spins, the individual values of q_k are smaller. Therefore, a larger value of Q_r is required to obtain the same response in S_4, which explains the difference between $\Omega_{1/2}$ for the same absolute value of Q_r in the simulations.

The main message of the section is that S_4 spectroscopy in larger magnetic field will open a new door to gain access on the distribution by measuring $\Omega_{1/2}(b_x)$. Although the absolute value of $\Omega_{1/2}(b_x)$ depends in detail on the distribution of the couplings q_k, studying the field-dependent width gives an indication of the average crossover scale from dominating quadrupolar interaction to a dominating nuclear Zeeman term [31–33].

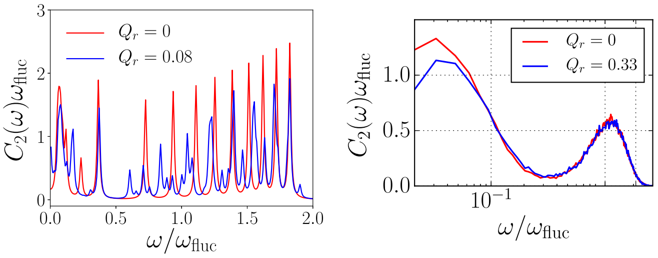

FIG. 13. Comparison of $C_2(\omega)$ with and without H_Q. The left panel shows the results of quantum-mechanical calculation, with $N = 1$, $I = 9/2$, and $Q_r = 0.08$, the right panel the classically computed spectrum using $N = 100$, $Q_r = 0.33$.

2. Fourth-order spin noise in the crossover regime

Now we turn to the crossover regime where the Zeeman energy is of the order of ω_{fluc}, i.e., $b_x \approx 1$. The electron spin dynamics is governed by the external magnetic field and the fluctuating Overhauser field, which have equal strength. Furthermore, the nuclear Zeeman energy is weak such that the nuclear spin dynamics is dominated by the nuclear-electric quadrupolar interaction in combination with the weak Knight field generated by the electron spin. We are interested in comparing two extreme limits: the dynamics of the smallest system one can imagine, including only a single nuclear spin, and the limit of large number of spins. While $N = 1$ requires a purely quantum-mechanical calculations, we mimic the large N limit with a classical simulation of $N = 100$ bath spins.

In this regime H_Q does not only influence S_4 but also modifies $C_2(\omega)$. The change of $C_2(\omega)$ induced by the quadrupolar interaction is depicted in Fig. 13 for bath sizes $N = 1$ (left panel) and $N = 100$ (right panel).

We use the corresponding spin noise C_2 to calculate the fourth-order cumulant. In Fig. 14 the classical and the quantum-mechanical results of S_4 are presented for $b_x = 1$. Note that the quantum-mechanical S_4 on the left computed in the limit of weak measurement for $N = 1$, is near identical to the S_4 presented for strong and continuous measurement in

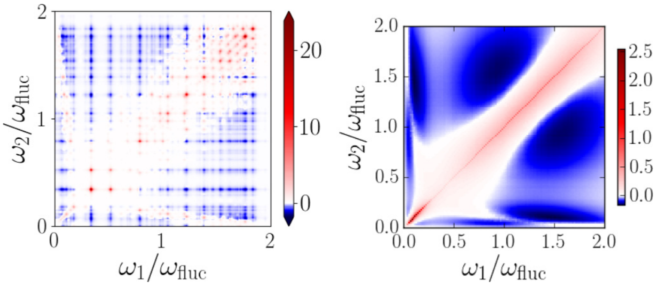

FIG. 14. S_4 for a smaller magnetic field of $b_x = 1$. Left is the quantum-mechanical calculation, with $N = 1$, $I = 9/2$, and $Q_r = 0.08$. On the right is the classically computed spectrum with $N = 100$, $Q_r = 0.33$.

Ref. [38]. For small ω_1 or ω_2 we also found alternating signs of correlations in the (ω_1, ω_2)-plane. Fixing $\omega_1/\omega_{\text{fluc}} = 1$ and increasing ω_2 reveals first weak anticorrelation (encoded in blue), then correlations (encoded in red) before switching back to anticorrelations. Also, the strong correlations are not confined to the diagonal as depicted in Fig. 7 but are significantly spread due to the presence of the quadrupolar couplings.

The classically obtained S_4 on the right shows the effects of quadrupolar coupling in small magnetic fields for a far bigger bath of $N = 100$, which results in a continuous spectrum with similar features. These are the anticorrelation contributions at the axis with a dip in anticorrelation along $\omega_{1/2}/\omega_{\text{fluc}} = 1$, as well as the broadening of the correlation on the diagonal.

3. Discussion

While the second-order spin correlation function $C_2(t)$ decays fast on the time scale T^* in finite magnetic field that long-time effects of nuclear quadrupolar coupling cannot be observed in the electron spin dynamics, they modify the frequency characteristics of the fourth-order spin correlation function significantly. The positive correlations in the spin noise power bispectrum that are pinned to the frequency diagonal in the CSM are broadened and acquire a finite width proportional to the nuclear coupling strength at a large magnetic field.

With and without quadrupolar interaction the classical and the quantum mechanical method yield congruent results for the second-order correlation. The same is true for the fourth-order correlation without quadrupolar interaction. If quadrupolar interaction is introduced, both the classical and quantum-mechanical method show qualitatively similar behavior: a broadening of the correlation peak along the $\omega_1 + \omega_2 = \text{const.}$ cut. But, as can be seen in Fig. 9, the spectra of different methods exhibit a quantitatively different curve progression, and to not follow the same scaling behavior presented in Sec. V B. This shows that the fourth-order correlation yields uniquely quantum-mechanical information that appears with the introduction of quadrupolar interaction into the system, as has been previously shown in Ref. [33].

It is straightforward to extend the investigation to an arbitrary angle between the z axis and the applied magnetic field. This is a well-studied problem in the context of the standard SNS and it turns out that a tilted magnetic field does not provide additional new information. Therefore, we do not include these results in this paper. For the limiting case of a single bath spin, i.e., $N = 1$, we refer to Fig. 6 in Ref. [38], which extrapolated to continuous spectra as obtained with our classical simulation.

VI. CONCLUSION

We presented a combination of a quantum-mechanical and a classical simulation to the fourth-order noise correlation function, to calculate the spin-noise power bispectrum in a quantum dot in the presence of the nuclear-electric quadrupolar interaction in the limit of a very small and a very large nuclear spin bath. Our approach is valid in the limit of a nearly perturbation-free off-resonance detection of the spin polarization in the quantum dot ensemble using the Faraday rotation of a weak linear polarized optical probe signal.

The second-order spin correlation function $C_2(t)$ is used as a gauge to connect the nuclear spin length I and the effective quadrupolar interaction strength Q_r to the number of nuclear spins of the spin bath in all calculations. To account for the effect of quadrupolar interaction in a classical spin dynamics, we derived a modification of the effective Knight field in classical equations of motions.

The quantum-mechanical and the classical spin-noise bispectrum agree well for the CSM. The quantum-mechanical bispectrum converges to the result of the classical simulation for large nuclear spin bath and large nuclear spin length. In both cases the quantum-mechanical eigenvalue spectrum approaches a continuum distribution. Interestingly, already relatively small spin baths provide a good representation of a larger bath bispectrum.

The fourth-order cumulant S_4 is made up of two basic building blocks: $C_4(\omega_1, \omega_2)$ and $C_2(\omega_1)C_2(\omega_2)$. The decomposition of those parts show that the product of the second-order spin noise gives a two-dimensional Gaussian, which is solely responsible for anticorrelation in the spectrum while C_4 is nonzero only on the diagonal in the CSM.

Adding the quadrupolar interaction term H_Q to the CSM is causing a broadening of C_4 across the diagonal. The width of this broadening is directly proportional to the quadrupolar coupling strength at small couplings and a finite magnetic field. The width could be used as a direct experimental probe of the average quadrupolar interaction strength in a sample. The near perfect agreement observed in $C_2(\omega)$ between the classical and the quantum-mechanical simulations is slightly modified in the bispectrum. The qualitative agreement between the bispectra of both methods with comparable parameters is remarkable concerning the location of the correlation as well as the anticorrelations. The broadening of the quantum-mechanical spectra C_4 along the diagonal, however, is more pronounced than in its classical counterpart, while the decrease of the amplitude due to quadrupolar interaction is stronger for the results of the classical method. The difference in the shape between the results of both methods becomes visible in the cut through the diagonal.

We have proven that the simple linear response theory to higher correlation functions [34,35] produces congruous results to those obtained with an elaborate weak measurement theory presented in Ref. [38]. This shows that the assumption of a nonperturbative measurement yields identical results that the weak measurement theory in the weak coupling limit [38].

ACKNOWLEDGMENTS

We acknowledge the financial support by the Deutsche Forschungsgemeinschaft and the Russian Foundation of Basic Research through the Transregio TRR 160 project A7, and we thank Daniel Hägele and Manfred Bayer for the fruitful discussions. The authors gratefully acknowledge the computing time granted by the John von Neumann Institute for Computing (NIC) under project HDO09 and provided on the supercomputers JUWELS and JURECA at the Jülich Supercomputing Centre.

[1] N. A. Sinitsyn and Y. V. Pershin, Rep. Prog. Phys. **79**, 106501 (2016).

[2] E. B. Aleksandrov and V. S. Zapasskii, Zh. Eksp. Teor. Fiz. **81**, 132 (1981) [JETP **54**, 64 (1981)].

[3] V. S. Zapasskii, Adv. Opt. Photon. **5**, 131 (2013).

[4] S. A. Crooker, D. G. Rickel, A. V. Balatsky, and D. L. Smith, Nature (London) **431**, 49 (2004).

[5] M. Oestreich, M. Römer, R. J. Haug, and D. Hägele, Phys. Rev. Lett. **95**, 216603 (2005).

[6] S. A. Crooker, L. Cheng, and D. L. Smith, Phys. Rev. B **79**, 035208 (2009).

[7] F. Berski, J. Hübner, M. Oestreich, A. Ludwig, A. D. Wieck, and M. Glazov, Phys. Rev. Lett. **115**, 176601 (2015).

[8] R. Hanson, L. P. Kouwenhoven, J. R. Petta, S. Tarucha, and L. M. K. Vandersypen, Rev. Mod. Phys. **79**, 1217 (2007).

[9] A. Bechtold, D. Rauch, F. Li, T. Simmet, P. Ardelt, A. Regler, K. Muller, N. A. Sinitsyn, and J. J. Finley, Nature Phys. **11**, 1005 (2015).

[10] G. S. Uhrig, J. Hackmann, D. Stanek, J. Stolze, and F. B. Anders, Phys. Rev. B **90**, 060301(R) (2014).

[11] S. A. Crooker, J. Brandt, C. Sandfort, A. Greilich, D. R. Yakovlev, D. Reuter, A. D. Wieck, and M. Bayer, Phys. Rev. Lett. **104**, 036601 (2010).

[12] Y. Li, N. Sinitsyn, D. L. Smith, D. Reuter, A. D. Wieck, D. R. Yakovlev, M. Bayer, and S. A. Crooker, Phys. Rev. Lett. **108**, 186603 (2012).

[13] P. Glasenapp, D. S. Smirnov, A. Greilich, J. Hackmann, M. M. Glazov, F. B. Anders, and M. Bayer, Phys. Rev. B **93**, 205429 (2016).

[14] J. Hackmann and F. B. Anders, Phys. Rev. B **89**, 045317 (2014).

[15] J. Hackmann, P. Glasenapp, A. Greilich, M. Bayer, and F. B. Anders, Phys. Rev. Lett. **115**, 207401 (2015).

[16] N. Wu, N. Fröhling, X. Xing, J. Hackmann, A. Nanduri, F. B. Anders, and H. Rabitz, Phys. Rev. B **93**, 035430 (2016).

[17] N. A. Sinitsyn, Y. Li, S. A. Crooker, A. Saxena, and D. L. Smith, Phys. Rev. Lett. **109**, 166605 (2012).

[18] P. Glasenapp, N. A. Sinitsyn, L. Yang, D. G. Rickel, D. Roy, A. Greilich, M. Bayer, and S. A. Crooker, Phys. Rev. Lett. **113**, 156601 (2014).

[19] M. Poggio, H. J. Mamin, C. L. Degen, M. H. Sherwood, and D. Rugar, Phys. Rev. Lett. **102**, 087604 (2009).

[20] C. L. Degen, M. Poggio, H. J. Mamin, and D. Rugar, Phys. Rev. Lett. **99**, 250601 (2007).

[21] D. K. Young, J. A. Gupta, E. Johnston-Halperin, R. Epstein, Y. Kato, and D. D. Awschalom, Semicond. Sci. Technol. **17**, 275 (2002).

[22] N. Jäschke, F. B. Anders, and M. M. Glazov, Phys. Rev. B **98**, 045307 (2018).

[23] A. Greilich, R. Oulton, E. A. Zhukov, I. A. Yugova, D. R. Yakovlev, M. Bayer, A. Shabaev, A. L. Efros, I. A. Merkulov, V. Stavarache, D. Reuter, and A. Wieck, Phys. Rev. Lett. **96**, 227401 (2006).

[24] A. Greilich, D. R. Yakovlev, A. Shabaev, A. L. Efros, I. A. Yugova, R. Oulton, V. Stavarache, D. Reuter, A. Wieck, and M. Bayer, Science **313**, 341 (2006).

[25] N. Jäschke, A. Fischer, E. Evers, V. V. Belykh, A. Greilich, M. Bayer, and F. B. Anders, Phys. Rev. B **96**, 205419 (2017).

[26] S. Varwig, E. Evers, A. Greilich, D. R. Yakovlev, D. Reuter, A. D. Wieck, T. Meier, A. Zrenner, and M. Bayer, Appl. Phys. B **122**, 17 (2016).

[27] L. M. Norris, G. A. Paz-Silva, and L. Viola, Phys. Rev. Lett. **116**, 150503 (2016).

[28] P. Szańkowski, G. Ramon, J. Krzywda, D. Kwiatkowski, and Ł. Cywiński, J. Phys.: Condens. Matter **29**, 333001 (2017).

[29] I. A. Merkulov, A. L. Efros, and M. Rosen, Phys. Rev. B **65**, 205309 (2002).

[30] C. Testelin, F. Bernardot, B. Eble, and M. Chamarro, Phys. Rev. B **79**, 195440 (2009).

[31] D. Press, K. De Greve, P. L. McMahon, T. D. Ladd, B. Friess, C. Schneider, M. Kamp, S. Höfling, A. Forchel, and Y. Yamamoto, Nature Photon. **4**, 367 (2010).

[32] A. Bechtold, F. Li, K. Müller, T. Simmet, P.-L. Ardelt, J. J. Finley, and N. A. Sinitsyn, Phys. Rev. Lett. **117**, 027402 (2016).

[33] N. Fröhling and F. B. Anders, Phys. Rev. B **96**, 045441 (2017).

[34] F. Li, A. Saxena, D. Smith, and N. A. Sinitsyn, New J. Phys. **15**, 113038 (2013).

[35] F. Li and N. A. Sinitsyn, Phys. Rev. Lett. **116**, 026601 (2016).

[36] G. Chen, D. L. Bergman, and L. Balents, Phys. Rev. B **76**, 045312 (2007).

[37] D. Stanek, C. Raas, and G. S. Uhrig, Phys. Rev. B **90**, 064301 (2014).

[38] D. Hägele and F. Schefczik, Phys. Rev. B **98**, 205143 (2018).

[39] R. Kubo, J. Phys. Soc. Jpn. **17**, 1100 (1962).

[40] C. H. Bennett and D. P. DiVincenzo, Nature (London) **404**, 247 (2000), review Article.

[41] G. Burkard, H.-A. Engel, and D. Loss, Fortschr. Phys. **48**, 965 (2000).

[42] D. Loss and D. P. DiVincenzo, Phys. Rev. A **57**, 120 (1998).

[43] M. Gaudin, J. Phys. **37**, 1087 (1976).

[44] W. A. Coish and D. Loss, Phys. Rev. B **70**, 195340 (2004).

[45] K. A. Al-Hassanieh, V. V. Dobrovitski, E. Dagotto, and B. N. Harmon, Phys. Rev. Lett. **97**, 037204 (2006).

[46] M. M. Glazov and E. L. Ivchenko, Phys. Rev. B **86**, 115308 (2012).

[47] R. I. Dzhioev and V. L. Korenev, Phys. Rev. Lett. **99**, 037401 (2007).

[48] C. Bulutay, Phys. Rev. B **85**, 115313 (2012).

[49] J. M. Mendel, Proc. IEEE **79**, 278 (1991).

[50] A. Khintchine, Math. Ann. **109**, 604 (1934).

[51] Strictly speaking, the frequencies ω_i are multiples of $2\pi/T_m$ in a Fourier transformation on a finite interval $[-T_m/2, T_m/2]$ but are asymptotically dense for $T_m \to \infty$, so that we treat them as continuous variables with the proper mathematical limit implied.

[52] J. Hackmann, Ph.D. thesis, TU Dortmund, 2015, https://eldorado.tu-dortmund.de/handle/2003/28648.